Supplementary Information

Nature-inspired dynamic nanoconfinement enables life-like mechanical adaptability and robust environmental resilience in polyurethane-urea elastomers

Hao Wu[a, b*], Zhou Lu[a, b], Ming Jin[a, b], Junhao Xie[a, b], Jinqiu Tao[a, b], Chengjun Yue[a, b], Lei Dong[a, b] and Qianping Ran[a, b*]

[a] *Jiangsu Key Laboratory of Construction Materials, School of Materials Science and Engineering, Southeast University, Nanjing, Jiangsu,211189, P.R. China*

[b] *State Key Laboratory of Engineering Materials for Major Infrastructure, School of Materials Science and Engineering, Southeast University, Nanjing, Jiangsu,211189, P.R. China*

Corresponding author E-mail: hwu2018@ustc.edu; qpran@cnjsjk.cn

1. Experimental Section

1.1. General Characterization

FTIR spectra were collected by Thermal Fisher (Nicolet IS20) from 500 cm^{-1} to 4000 cm^{-1}. ^{1}H NMR spectroscopy was evaluated by Bruker VANCE III HD 600 MHz spectrometer at room temperature using a deuterated dimethyl sulfoxide solvent. The thermal transition behavior was studied on a DSC system in an N_2 atmosphere with temperature increasing from -100 °C to 80 °C at a heating rate of 10 °C min^{-1}. Dynamic mechanical analysis (DMA, TA Q800) was employed to characterize the viscoelastic properties of the elastomers, with the experiments conducted under a nitrogen atmosphere. The testing mode was set to tensile mode, with a loading frequency of 1 Hz and a heating rate of 5°C/min. XRD patterns were obtained by an X-ray diffraction analyzer (D8 Advance, Bruker, U.S.) using Cu Kα radiation (λ=0.1541 nm). The temperature dependence of the FTIR of the samples was characterized by variable temperature infrared spectroscopy (Thermo IS 50, Thermal Fisher, K-M transform) over a range from 20°C to 150°C, and the 2D Shige software was deployed to analyze the 2D infrared spectra of the resulting data. The cross-section morphology of samples at fracture was characterized by means of SEM (ZEISS Sigma 360).

1.2. Mechanical Test:

The mechanical tensile properties of the samples were examined through a series of tests conducted at ambient temperature using an MTS tester equipped with a 2000N transducer. The rate of tensile testing was set at 100 mm/min. The toughness index of

the samples was derived by integrating the area beneath the resulting stress-strain curve, while the Young's modulus of the samples was calculated from the initial slope of the stress-strain curve. The puncture resistance of the samples was characterized using a stainless-steel cylindrical probe with a diameter of 1.0 mm on a tensile testing machine，and Use a universal material testing machine to conduct cyclic tensile tests on materials and calculate the energy dissipation efficiency of each cycle to evaluate the effects of multiple hydrogen bonds and dynamic coordination on energy dissipation in materials. The puncture resistance of the samples in this experiment was measured using a biro tip, and the digital DIC (VIC-3D) technique was further used to investigate the stress transfer behavior of the BMSHPU-30 during the uniaxial tensile test. SAXS measurement was operated to detect alterations in the structural configuration of the samples prior to and following biomineralization. It was also instrumental in monitoring the progression of structural evolution in the BMSHPU-30 under varying degrees of stretching. In order to evaluate the self-healing performance of the elastomer, the BMSHPU-30 was firstly divided into two separate pieces and then reconnected under the assistance of solvent for varying time intervals. Stress-strain curves were recorded during this process to assess the healing efficiency. And the healing efficiency (η) is defined by the following equation:

$$\eta\ (\%) = (P_{healed} / P_{original}) \times 100\%$$

where P_{healed} and $P_{original}$ are the mechanical properties (tensile strength) of the healed and original virgin BMSHPU-30 sample, respectively.

Subsequent microscopic analysis was conducted to observe the healing state. Furthermore, the load bearing safety of the material post-damage repair was assessed by applying a weight to ascertain the structural integrity and recovery of the healed material.

1.3 The calculation of dynamic bond binding energy

All the calculations were calculated using Gaussian 09 program.[1] All monomers and dimers were optimized to the groåund (S0) state equilibrium by density functional theory (DFT) [2-3]. Geometry optimizations and frequency calculations were carried out at the B3LYP levels of theory with the 6–31G(d) basis set. To improve the description on the non-bond interactions between two monomers in a dimer, Grimme's D3BJ dispersion correction was also combined with the B3LYP fucntional (i.e. B3LYPD3 functionals). In order to eliminate the influence of Basis Set Superposition Error (BSSE) on the calculation accuracy of the interaction energy, at the M062X/def2-TZVP level of theory, we use the counterpoise correction (CP) method to calculate the energy error caused by the BSSE to obtain more accurate interaction energy: E(interaction)=E(AB)+E (BSSE)–E(A)–E(B).

1.4 All-atom molecular dynamics (MD) simulation

The deformation behaviors of PU polymer-CNCs-Zn nanocomposite are investigated from the molecular level using classic molecular dynamics (MD) simulations. To this end, MD box with dimensions of 70 × 70 × 130 $Å^3$ is generated, in which 20 PU polymer chains, 160 Zn^{2+}, 320 Cl^- and CNCs nanocrystal with dimensions of around 20 × 30 × 68 $Å^3$ are randomly placed. The PU polymer chain is composed of 10 polymer monomers. Periodic boundary conditions (PBCs) are imposed in the three orthogonal directions to mimic large XX- polymer nanocomposite sample. To describe the atomic interactions in the CNCs-Zn^{2+}-resin based nanocomposite, the Polymer Consistent Force Field (PCFF) is utilized. To describe the non-bonded interactions, the van der Waals (vdW) interactions are considered by the Lennard-Jones 9-6 potential with a cut-off distance of 12 Å, while the long-range electrostatic interactions are described by the standard Coulomb potential using the particle−particle−particle−mesh

(PPPM) algorithm. Prior to MD simulations, the configurations of the four XX-polymer-based samples are optimized to a local configuration with energy and force tolerances of 1.0×10^{-4} Kcal/mol and 1.0×10^{-4} Kcal/mol·Å, respectively. Then, as-optimized samples are relaxed at temperature of 500 K under isochoric isothermal (NVT) ensemble within 100,000 timesteps. Subsequently, the sample is further relaxed at temperature of 500 K with 100,000 timesteps subjected to confining pressure of 1 bar under isobaric-isothermal (NPT) ensemble, followed by cooling from 500 K to 300 K within 100,000 timesteps under NPT ensemble. Afterwards, MD simulations with another 100,000 timesteps are carried out at temperature of 300 K and confining pressure of 1 bar under isobaric-isothermal (NPT) ensemble to achieve relaxed sample. Finally, as-relaxed sample is uniaxially stretched with constant engineering rate of 1.0×10^{-6}/fs along the *x*-direction to examine the deformation behaviors. The dynamics of atoms in the XX-polymer-based systems follow the classical Newton's motion. The velocity-Verlet algorithm with timestep of 1.0 fs is utilized to integrate the classic Newton's equation. All the MD simulations are implemented using the Large-scale Atomic/Molecular Massively Parallel Simulator (LAMMPS) package.

1.5 Service assessment method in extreme environment

Conduct salt spray testing according to ASTM B117 standard to evaluate the durability of materials under harsh corrosion conditions in a simulated environment (35 ° C, ≥95% RH, with a 5% NaCl solution at pH 6.5-7.2).Tensile testing was conducted on the elastomer samples before and after exposure to measure the retention of tensile strength and elongation at break. The retention rate of these mechanical properties was calculated in order to evaluate the material's durability under extreme conditions. The solvent resistance of BMSHPU-30 was evaluated by subjecting the elastomer samples to immersion in a range of solvents, including pure water, ethanol, isopropanol,

acetonitrile, DMF, and tetrahydrofuran. The samples were stored in these solvents for a period of 150 days at ambient temperature. The solubility of the material was measured by calculating the mass loss and observing the dissolution behavior of the BMSHPU-30.

The antifouling performance of BMSHPU-30 was evaluated by conducting an inhibition zone test against *Pseudomonas aeruginosa*. Pure coating and BMSHPU-30 samples were exposed to *P. aeruginosa* cultures, and the inhibition zone was measured to determine the antibacterial activity. The inhibition zone size was compared between BMSHPU-30 and the pure coating to assess the material's ability to inhibit bacterial growth. The antibacterial activity of BMSHPU-30 was determined by exposing Pseudomonas aeruginosa cultures to the material and subsequently subjecting them to fluorescence staining to differentiate between live and dead bacteria. Fluorescent dyes were applied, with live bacteria emitting green fluorescence and dead bacteria emitting red fluorescence. Imaging of the bacterial cultures on both pure coating and BMSHPU-30 surfaces was conducted, and the number of live and dead bacterial cells was compared to evaluate the material's antibacterial effect. The quantification of antimicrobial efficiency was achieved by measuring the fluorescence intensity, and the percentage of bacterial growth inhibition was subsequently calculated.

2. Supplementary Figures and Tables

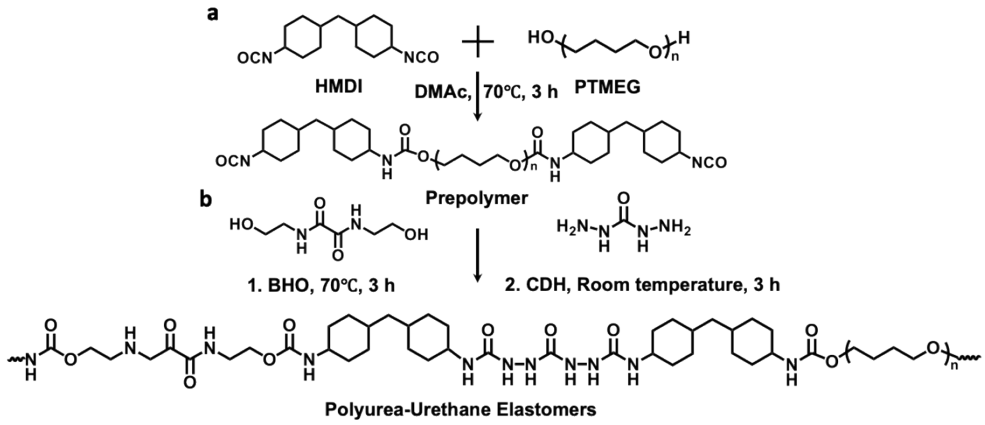

Figure S1 Schematic illustration of the synthetic route of SHPU.

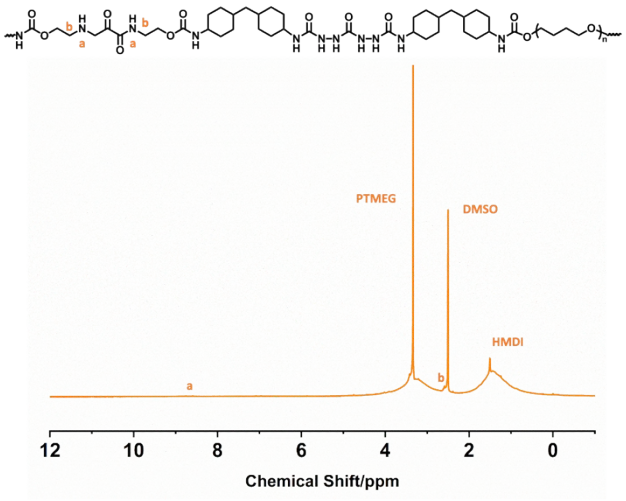

Figure S2 ^{1}H NMR spectrum of SHPU dissolved in deuterated DMSO.

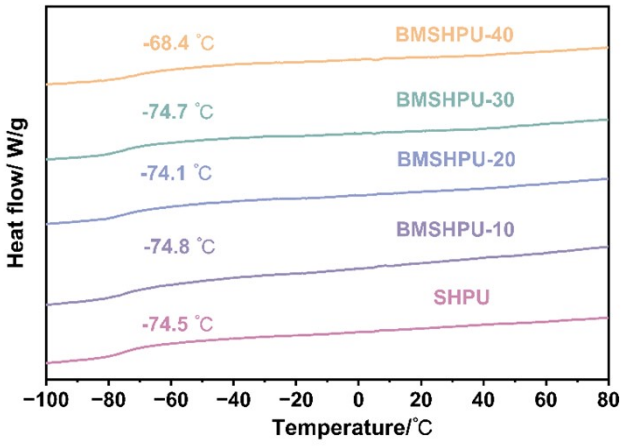

Figure S3 DSC curves of the SHPU and BMSHPU-X.

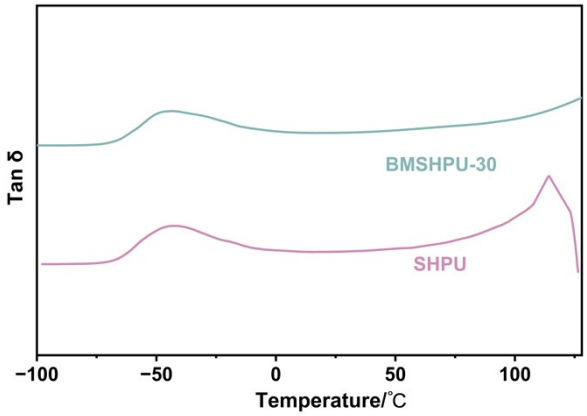

Figure S4 Tanδ curves of the SHPU and BMSHPU-30.

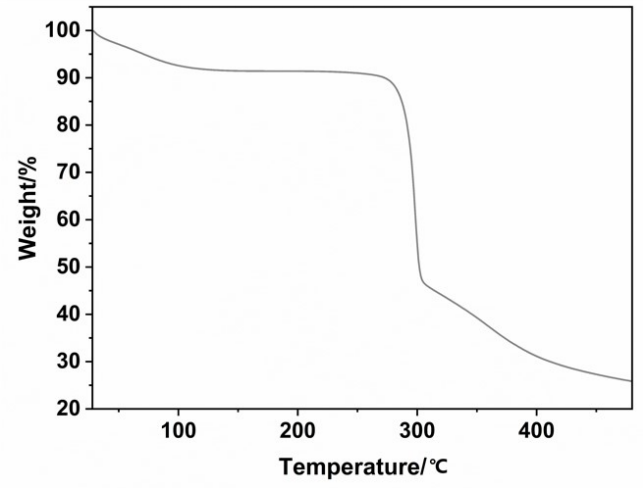

Figure S5 TGA curves of CNCs.

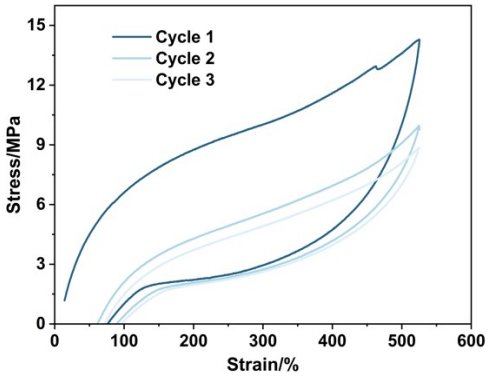

Figure S6 Cyclic tensile curve of BMSHPU-30 under a constant strain.

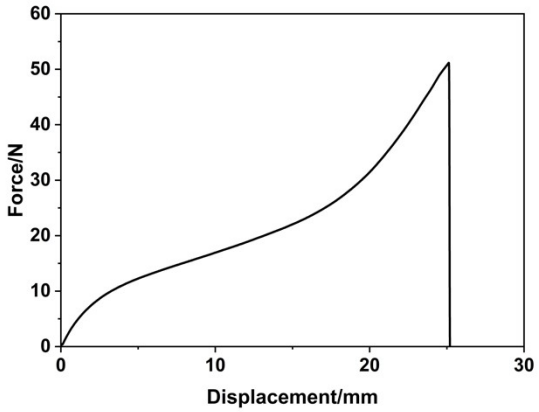

Figure S7 Force–displacement curve of BMSHPU-30 during the puncture resistance test.

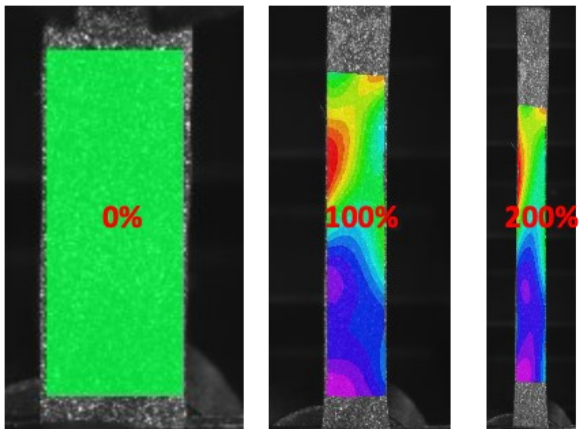

Figure S8 The SHPU was monitored using DIC technology during a pure tensile test.

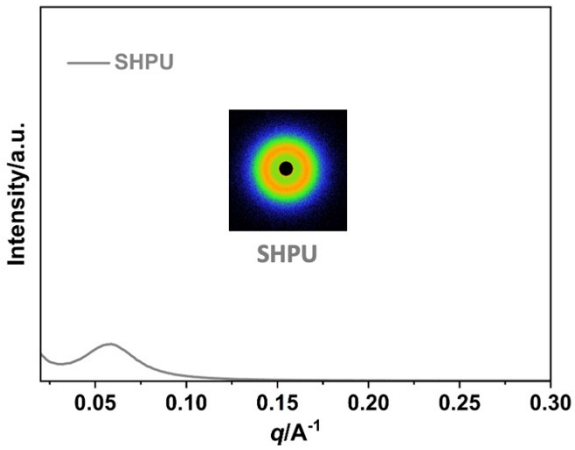

Figure S9 In situ 1D-WAXS patterns and 2D-SAXS integral curves for SHPU.

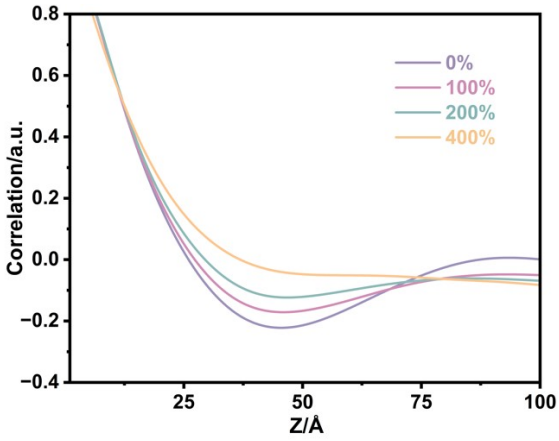

Figure S10 In situ SAXS-based one-dimensional correlation function normalization analysis of BMSHPU-30 during the stretching process.

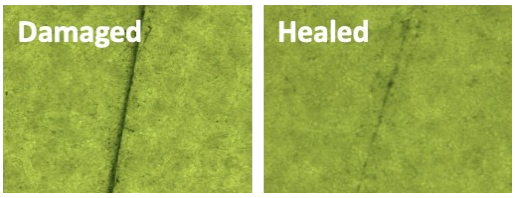

Figure S11 Healing process of the BMSHPU-30 was observed by the optical microscope.

Table S1 Summary of tensile strength, elongation at break, recovery efficiency and toughness of this work and some elastomer recently reported on literature.

Samples	Tensile strength (MPa)	Elongation at break(%)	Healing (%)	Toughness (MJ m^{-3})	Ref.
ATPU-20	17.46	1000	94.04	/	S1
WPUSS-P4	20.9	375	93	63.35	S2
MPUF3	37.11	702	91.8	/	S3
T/AG	46.6	1736.89	85.62	337.19	S4
SPU-$UPy_{0.5}$: Zn =1:1	14.15	477	95	47.57	S5
CRSP-3	7	1399	/	/	S6
DPUU-2000	84.2	925.6	/	322.8	S7
PDES-PEGDA	11.3	2396	/	28.18	S8
PPeF4-AOH15-R1.8	55.1	548	88.9	/	S9
PDES–EAN-b	30.6	320	85.7	65	S10
PUU-0.5	76.37	839.1	88.64	308.63	S11
FTD-C	23.5	/	/	219.93	S12
BMSHPU-30	71.5	2207	96%	663.87	This work

Type	Structure	The binding energy of the main dynamic bonds
H-bonds by N, N'-Bis(2-hydroxyethyl) oxamide	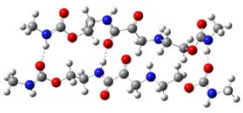	-19.46 kJ mol^{-1}
H-bonds by Carbohydrazide	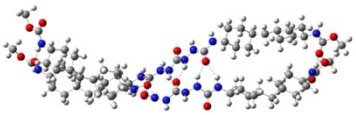	-45.58 kJ mol^{-1}
Coordination PU-Zn^{2+}-CNCs-Zn^{2+}-PU	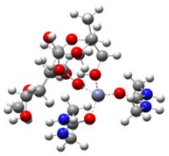	-420.79 kJ mol^{-1}

Figure S12 The interaction form models and the calculated binding energy values of groups are presented.

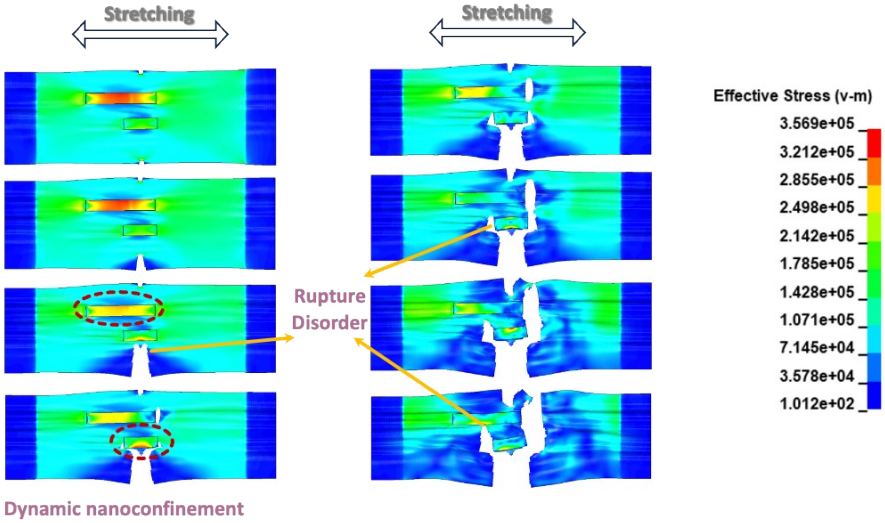

Figure S13 Schematic representation of the proposed finite element analysis of the strengthening mechanism of elastomer properties by dynamic nanoconfinement domain effect.

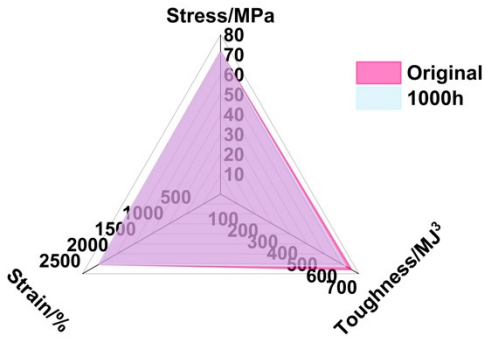

Figure S14 Image summarizes the changes in the stress, strain, and toughness of BMSHPU-30 after being treated with moisture.

Figure S15 Optical images of BMSHPU-30 after immersion in DMF and THF solvents.

References:

1. Y. Zhang, C. Zhang, Z. Cui, N. Li, Z. Ren and Z. Guan, *Polymer*, 2025, **322**.

2. B. Fu, Y. Wu, X. Cao, K. Wei and B. Shan, *Progress in Organic Coatings*, 2025, **203**.

3. S. Yang, S. Wang, X. Du, Z. Du, X. Cheng and H. Wang, *Chemical Engineering Journal*, 2020, **391**.

4. X. Zhu, Y. Hao, L.-F. Huang, H. Zhao and L. Wang, *Journal of Materials Chemistry A*, 2024, **12**, 26158-26169.

5. J. Xu, X. Wang, X. Zhang, Y. Zhang, Z. Yang, S. Li, L. Tao, Q. Wang and T. Wang, *Chemical Engineering Journal*, 2023, **451**.

6. C. Li, C. Jike, Y. Song, G. L. Li, Y. Jia and J. Li, *Advanced Functional Materials*, 2025, DOI: 10.1002/adfm.202507220.

7. X. Wang, J. Xu, X. Zhang, Z. Yang, Y. Zhang, T. Wang and Q. Wang, *Advanced Materials*, 2022, **34**.

8. Y. Lv, C. Li, Z. Yang, M. Gan, Y. Wang, M. Lu, X. Zhang and L. Min, *Advanced Science*, 2024, **11**.

9. D. Sun, J. Mo, W. Liu, N. Yan and X. Qiu, *Advanced Functional Materials*, 2024, **34**.

10. N. Wang, X. Yang and X. Zhang, *Nature Communications*, 2023, **14**.

11. X. Wang, J. Xu, Y. Zhang, T. Wang, Q. Wang, S. Li, Z. Yang and X. Zhang, *Nature Communications*, 2023, **14**.

12. J. Zhang, M. Zhang, H. Wan, J. Zhou and A. Lu, *Nature Communications*, 2025, **16**.